Broadband, electrically tuneable, third harmonic generation in graphene

Giancarlo Soavi[1], Gang Wang[1], Habib Rostami[2], David Purdie[1], Domenico De Fazio[1], Teng Ma[1], Birong Luo[1], Junjia Wang[1], Anna K. Ott[1], Duhee Yoon[1], Sean Bourelle[1], Jakob E. Muench[1], Ilya Goykhman[1], Stefano Dal Conte[3,4], Michele Celebrano[4], Andrea Tomadin[2], Marco Polini[2], Giulio Cerullo[3,4], Andrea C. Ferrari[1]

[1]Cambridge Graphene Centre, University of Cambridge, Cambridge CB3 0FA, UK
[2]Istituto Italiano di Tecnologia, Graphene Labs, Via Morego 30, I-16163 Genova, Italy
[3]IFN-CNR, Piazza L. da Vinci 32, I-20133 Milano, Italy
[4]Dipartimento di Fisica, Politecnico di Milano, Piazza L. da Vinci 32, I-20133 Milano, Italy

Optical harmonic generation occurs when high intensity light ($> 10^{10}\mathbf{W/m^2}$) interacts with a nonlinear material. Electrical control of the nonlinear optical response enables applications such as gate-tuneable switches and frequency converters. Graphene displays exceptionally strong-light matter interaction and electrically and broadband tuneable third order nonlinear susceptibility. Here we show that the third harmonic generation efficiency in graphene can be increased by almost two orders of magnitude by controlling the Fermi energy and the incident photon energy. This is due to logarithmic resonances in the imaginary part of the nonlinear conductivity arising from resonant multi-photon transitions. Thanks to the linear dispersion of the massless Dirac fermions, gate controllable third harmonic enhancement can be achieved over an ultrabroad bandwidth, paving the way to electrically-tuneable broadband frequency converters for applications in optical communications and signal processing.

The response of a material to interaction with an optical field can be described by its polarization [1]:

$$\vec{P} = \epsilon_0[\chi^{(1)} \cdot \vec{E} + \chi^{(2)} : \vec{E}\vec{E} + \chi^{(3)} \vdots \vec{E}\vec{E}\vec{E} + \cdots] \quad (1)$$

where $\vec{E}$ is the incident electric field and ϵ_0 is the permittivity of free space. $\chi^{(1)}$(dimensionless) is the linear susceptibility, while the tensors $\chi^{(2)}$ [m/V] and $\chi^{(3)}$ [m^2/V^2] are the second- and third-order nonlinear susceptibilities. The second and third order nonlinear optical susceptibilities are often reported in electrostatic units (esu), where the relation between esu and standard units (SI) can be described as follows [2]: $\chi^{(n)}(SI)/\chi^{(n)}(esu) = 4\pi/(3 \times 10^4)^{n-1}$. Thanks to the nonlinear terms of $\vec{P}$, new frequencies can be produced due to harmonic generation [3] and frequency mixing [4]. E.g., in Second Harmonic Generation (SHG) an incident electromagnetic wave with angular frequency $\omega_0 = 2\pi\nu$, with ν the photon frequency, provides via $\chi^{(2)}$ a new electromagnetic wave with angular frequency $2\omega_0$ [3]. The SHG efficiency (SHGE) is defined as the ratio between the SH intensity and the intensity of the incoming light. Analogously, Third Harmonic Generation (THG) is the emission of a photon with energy triple that of the incident one. The THG efficiency (THGE) is defined as the ratio between the TH intensity and the intensity of the incoming light. Second-order nonlinear processes are also known as three-wave-mixing, as they mix two optical fields to produce a third one [5]. Third-order nonlinear processes are known as four-wave-mixing (FWM) [5], as they mix three fields to produce a fourth one.

Nonlinear optical effects are exploited in a variety of applications, including laser technology [6], material processing [7] and telecommunications [8]. E.g., to create new photon frequencies (532nm from SHG in a Nd:YAG laser at 1064nm) [9] or broadly tuneable ultrashort pulses (fs-ps) in optical parametric amplifiers (OPAs) [10] and optical parametric oscillators (OPOs) [11]. High harmonic generation is also used for extreme UV light [12] and attosecond pulse generation [13], while difference frequency generation is used to create photons in the THz range [14]. The ability to cover a large fraction of the electromagnetic spectrum, from UV to THz, is crucial in optical spectroscopy, because different energy regions can probe different features of a material (e.g. THz light can probe vibrational sub-levels as well as free electrons in the conduction/valence bands, vis and near-IR light can probe interband transitions, mid-IR can probe phonons, UV can be used for photoemission spectroscopy for the study of core electronic levels). In telecommunications, frequency conversion for Wavelength Division Multiplexing (WDM) is based on nonlinear effects, such as FWM [8].

Second order nonlinear effects can only occur in materials without inversion symmetry, while third order ones are present in any system independent of symmetry [1], and they thus are the main intrinsic nonlinear response for most materials. THG and SHG intensity enhancement was achieved by exploiting magnetic dipole [15] and excitonic resonances [16], surface plasmons in Ag films [17], plasmonic nanocavities [18] and photonic-crystal waveguides [19], by spatial compression of the optical energy, resulting in an increase of the local optical field. Nonlinear optical effects depend on the characteristics of the impinging light beam(s) (frequency, polarization and intensity) and on the properties of the nonlinear material, dictated by its electronic structure. The ability to electrically control the nonlinear optical response of a material by a gate voltage opens up disruptive applications in compact nanophotonic devices with novel functionalities. However, to the best of our knowledge, external electrical control of the THGE has not been reported to date.

Layered materials (LMs) have a strong nonlinear optical response [20, 23–29]. Electrically tuneable SHG was reported for monolayer WSe_2 for photon energies close to the A exciton ($\sim$1.66eV) [20]. However, the tunability was limited to a narrow band ($\sim$10meV) in the proximity of the excitonic transition. Electrically tuneable SHG was also achieved by inversion symmetry breaking in bilayer MoS_2 close to the C exciton ($\sim$2.75eV) [27], but SHGE was strongly dependent on the laser detuning with respect to the C exciton transition energy. Thus, in both cases electrical control was limited to narrow energy bands ($\sim$10-100meV) around the excitonic transitions. Graphene, instead, has electrically tuneable nonlinearities over a much broader bandwidth thanks to the linear dispersion of the Dirac Fermions. In single layer graphene (SLG), SHG is forbidden due to symmetry [30–33]. SHG was reported in the presence of an electric current [32, 33], but was found to be at least one order of magnitude weaker with respect to third-order nonlinear effects. Thus, third order nonlinear effects are the most intense terms of the intrinsic nonlinear optical response of SLG.

Third order nonlinearities in SLG were studied both theoretically [21, 22, 34, 35] and experimentally [23, 36, 37]. Ref.23 reported a $1/\omega_0^4$ dependence of the third order response in a narrow band (emitted photons between$\sim$1.47 and 1.63eV), but no resonant behavior nor doping dependence. Ref.37 reported a factor$\sim$2 enhancement in a FWM experiment at the onset of interband transitions ($\hbar\omega_0$=2$|E_F|$, where E_F is the Fermi Energy) for SLG on SiN waveguides in a narrow band (emitted photons between$\sim$0.79 and 0.8eV). Thus, to date, evidence of tuneable third order nonlinear effects in SLG is limited to narrow bands and weak enhancements.

Samples preparation and characterization. In order to test both the

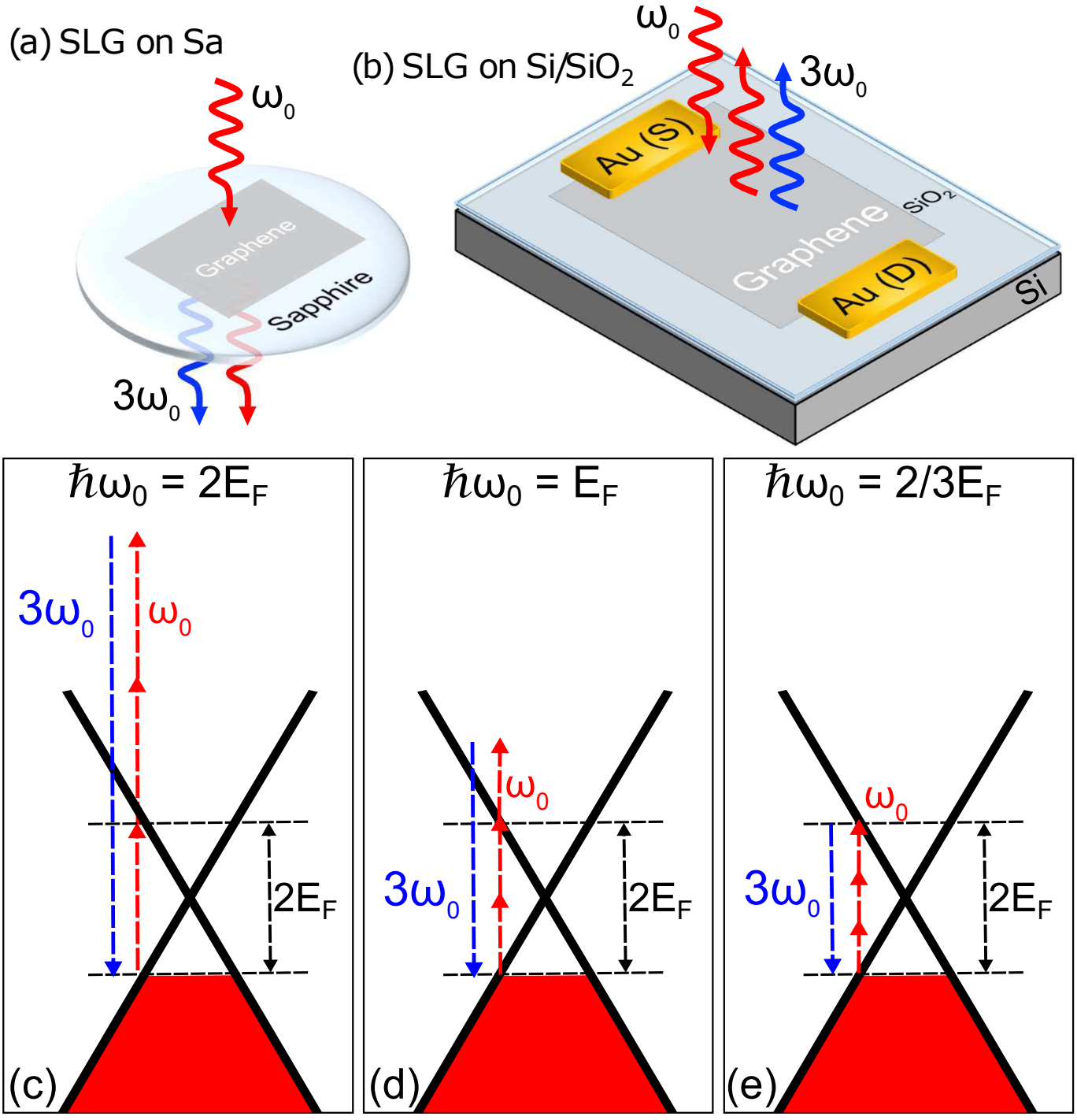

Figure 1: **THG measurements configurations and multi-photon resonances in SLG.** (a) CVD SLG on Sa for transmission. (b) Exfoliated SLG on Si/SiO_2 for reflection, with source (S) and drain (D) Au gates. (c-e) Resonances corresponding to the 3 logarithmic peaks in the imaginary part of the SLG nonlinear conductivity at T_e=0K for c) $\hbar\omega_0 = 2|E_F|$, d) $|E_F|$, e) $2|E_F|/3$. The red arrows represent the incident ω_0 photons and the blue ones the TH photons at $3\omega_0$.

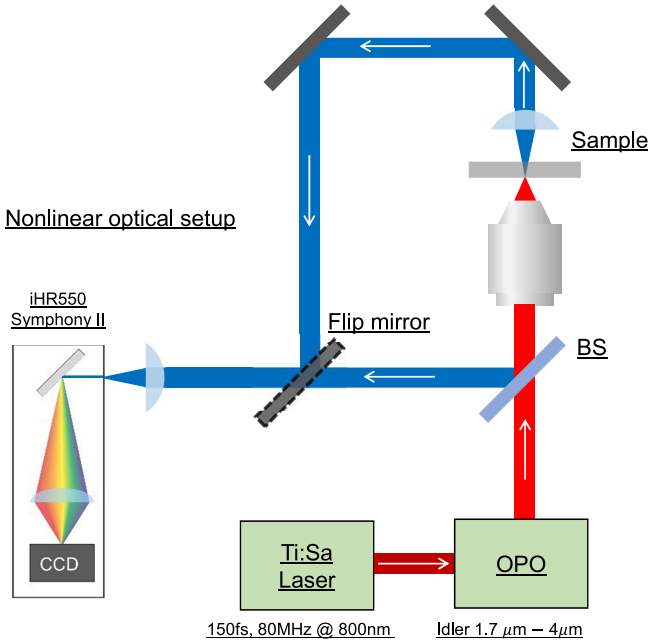

Figure 2: **Setup used for THG experiments**. A Ti:Sa mode-locked laser produces pulses at 800nm that seed an OPO. For THG experiments we use the OPO idler beam, tuneable between$\sim$1.7 and 4μm. This is aligned with a microscope and focused on the sample. The THG signal can be collected either in transmission or reflection with an iHR550 Horiba spectrometer coupled wth a Symphony II detector (Horiba). We use as a detector a liquid N_2 cooled CCD open electrode (OE) with 1024x256 pixels. BS, Beam Splitter.

photon energy dependence and the electrical tunability of THGE we use two sets of samples: SLG placed on a transparent substrate (sapphire, Sa), Fig.1a, and back-gated SLG on a reflective substrate (Si/SiO_2), Fig.1b. To study the THGE photon energy dependence, we measure it over a broad range (incident photon energy$\sim$0.4-0.7eV, with a THG signal at$\sim$1.2-2.1eV, limited by the absorption of our Si based charge-coupled device, CCD). Transmission measurements allow us to derive the absolute THGE, by taking into account the system losses and by minimizing the chromatic aberrations of the optical components (e.g. in reflection one needs to use beam splitters and these do not have a flat response over the$\sim$0.4-2.2eV range). Thus, we use chemical vapor deposition (CVD) to obtain a large area SLG ($\sim$cm size) and simplify the alignment, given the low optical contrast of SLG on Sa [38]. When measuring the THGE electrical tunability we need to follow the THG intensity normalized to its minimum, as function of gate voltage (V_G). For each ω_0 we measure THG spectra as a function of V_G. For each spectrum we calculate the total number of counts on the CCD, which is proportional to the number of THG photons, and divide all the spectra by that with the minimum counts. The key here is a precise control of E_F, while any system uncertainties on the absolute THGE are removed by the normalization. Thus, we use an exfoliated SLG back-gated field-effect transistor (FET) on Si+285nm SiO_2. A sketch of the experimental setup used for THG experiments, in transmission and reflection mode, is shown in Fig.2.

The two sets of samples are prepared and characterized as described in Methods. E_F for the CVD SLG on Sa is$\sim$250meV, and$<$100meV in the exfoliated SLG on Si+285nm SiO_2. The defect density is n_D $\sim 6\times10^{10}cm^{-2}$ for SLG on Sa and$\sim 2.4\times10^{10}cm^{-2}$ for SLG on Si/SiO_2. The small variation in defects suggests that the samples are comparable. Also, as discussed later, THGE has a negligible dependence on disorder, impurities and imperfections over a range of values representing the vast majority of SLGs in literature.

Photon energy dependence. The THGE measurements are performed in air at room temperature (RT) for both transmission and reflection. The THG signal is recorded with an iHR550 Horiba spectrometer coupled with a CCD detector (Symphony II, Horiba), as detailed in Methods and in Fig.2. Fig.3a plots representative TH spectra for different incident $\hbar\omega_0$ for SLG on Sa (Fig.1b) after calibration based on the photon-energy dependent losses of the setup, as described in Methods. We assign the measured signal to THG because the energy of the detected photons is three times the incident one ($\hbar\omega_{THG} = 3\hbar\omega_0$), and its intensity scales with the cube of the incident power ($I_{3\omega_0} \propto I^3_{\omega_0}$) [1], see Supplementary Fig.1. Fig.3b shows that when $\hbar\omega_0$ decreases from$\sim$ 0.7 to$\sim$ 0.4eV, THGE is enhanced by a factor$\sim$75. This depends on E_F and T_e. In the limit of E_F=0 and T_e=0 the third order optical

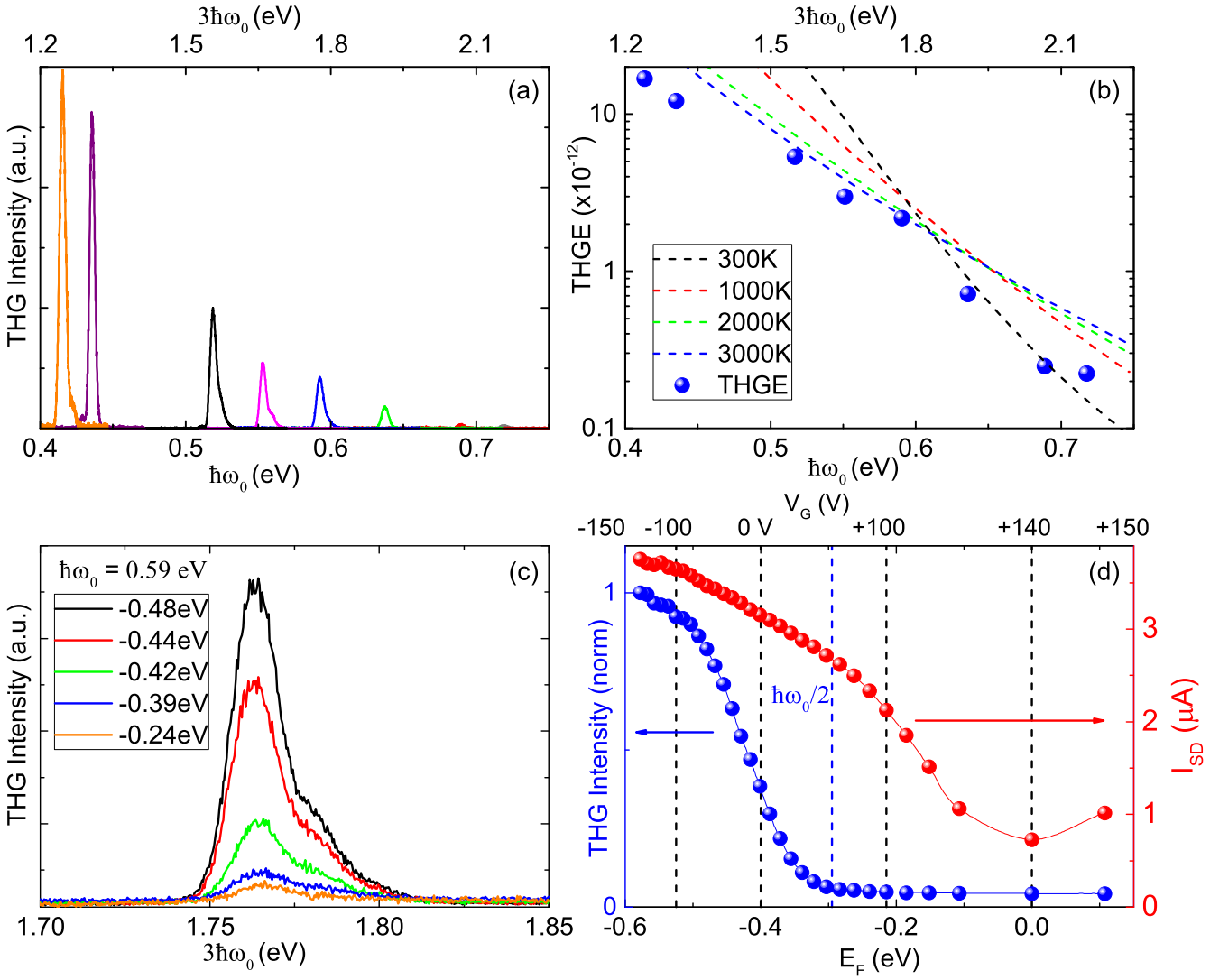

Figure 3: **Energy dependence and gate tunability of THG** (a) THG spectra for SLG on Sa (Fig.1b) for $\hbar\omega_0 \sim 0.4$ to$\sim$ 0.7eV and an average incident power$\sim$1mW. (b) THGE for SLG on Sa (Fig.1b) as a function of $\hbar\omega_0$ (x bottom axis) and $3\hbar\omega_0$ (x top axis). Curves are calculated for $\tau \gg$1ps and increasing T_e for E_F=250meV and $I_{\omega_0} \sim 2.4 \times 10^{12}$Wm^{-2}. (c) THG spectrum as a function of E_F for exfoliated SLG on Si/SiO$_2$ (Fig.1c) for $\hbar\omega_0 = 0.59$eV. (d) THG intensity (left y axis, blue dots) and source-drain current (I_{SD}) (right y axis, red dots) as a function of E_F (bottom x axis) and corresponding V_G (top x axis) for SLG on Si/SiO$_2$, Fig.1c

conductivity scales as $1/(\hbar\omega_0^4)$ [22]. In our case, E_F ∼250meV, and experiments are performed at RT. We explain this enhancement in the following paragraphs, by taking into account the dependence of the third order optical conductivity $\sigma^{(3)}_{\ell\alpha_1\alpha_2\alpha_3}$, where ℓ and $\alpha_{i=1,2,3}$ are Cartesian indexes, on ω_0, E_F and electronic temperature (T_e). Qualitatively, the expected THGE dependence on incident photon energy and E_F can be understood as follows. The linear optical response of SLG at T_e=0K has a "resonance" for $\hbar\omega_0 = 2|E_F|$, the onset of intra- and inter-band transitions [39]. Around this energy, a jump occurs in the real part of $\sigma^{(3)}_{\ell\alpha_1\alpha_2\alpha_3}$, due to the relaxation of the Pauli blocking constraint for vertical transitions between massless Dirac bands. From the Kramers-Kronig relations, this jump corresponds to a logarithmic peak in the imaginary part of $\sigma^{(3)}_{\ell\alpha_1\alpha_2\alpha_3}$. In a similar way, for the SLG third-order nonlinear optical response, logarithmic peaks in the imaginary part of $\sigma^{(3)}_{\ell\alpha_1\alpha_2\alpha_3}$ occur at T_e=0K for multi-photon transitions such that $m\ \hbar\omega = 2|E_F|$ with m=1,2,3, which correspond to incident photon energies $\hbar\omega_0 = 2|E_F|$, $|E_F|$, $2/3|E_F|$ [21, 22], as sketched in Fig.1c-e. At high T_e, due to the broadening of the Fermi-Dirac distribution, these peaks are smeared and merge, as derived in Supplementary Information Sect.S2. A comparison between theoretical curves, for E_F=250meV and different T_e, and experiments is plotted in Fig.3b. This indicates that both T_e and E_F play a key role, in particular when $\hbar\omega_0 \leq 2|E_F|$. The effects of disorder, impurities and imperfections can be phenomenologically introduced by a relaxation rate, $\Gamma = \hbar/\tau$, through the density matrix approach [21,34]. Our analysis (see Supplementary Information Sect.S2.3 and Supplementary Fig.4) shows that the effect on THGE of τ in the range∼0.1fs to ≫1ps is negligible. Thus, we can use ideal SLG in our theory, i.e. defect-free, with $\tau \gg$1ps, which simplifies the calculations.

Gate tuneability. Refs.21, 22 predicted that gate tuneability of THGE should be possible. Fig.3c plots the THG spectra for different V_G and $\hbar\omega_0$=0.59eV. Fig.3d shows the THG intensity over -600meV≤ E_F ≤+150meV corresponding to-150V≤ V_G ≤+150V. E_F is derived from each V_G as discussed in Methods. Fig.3d indicates that, as a function of V_G, there is a THG intensity enhancement by over a factor of 20 starting when $\hbar\omega_0 < 2|E_F|$. Fig.3d also suggests that THGE in SLG follows an opposite trend compared to FWM [37]: it is higher for intra-band ($\hbar\omega_0 < 2|E_F|$) than inter-band ($\hbar\omega_0 > 2|E_F|$) transitions. This is consistent with our calculations in Supplementary Information Sect.S2. For both transmission and reflection, the THGE for SLG, considered as a nonlinear interface layer between air and substrate, under normal incidence can be written as (see Supplementary In-

formation Sect.S2.1 and Supplementary Fig.2,3):

$$\eta^{THG}(\omega_0, E_F, T_e) = \frac{I_{3\omega_0}}{I_{\omega_0}} = f(\omega_0)\frac{I^2_{\omega_0}}{4\epsilon_0^4 c^4}\left|\sigma^{(3)}_{\ell\ell\ell\ell}(\omega_0, E_F, T_e)\right|^2 \quad (2)$$

where $\epsilon_0 \sim 8.85\times10^{-12}\mathrm{C(Vm)}^{-1}$ and $c = 3\times10^8\mathrm{m/s}$ are the vacuum permittivity and the speed of light; $f(\omega_0) = n_1^{-3}(\omega_0)n_2(3\omega_0)[n_1(3\omega_0) + n_2(3\omega_0)]^{-2}$ in which $n_{i=1,2}(\omega)$ is the refractive index of air (i=1) and substrate (i=2). For SLG on any substrate $n_1(\omega) \sim 1$ and $n_2(\omega) = \sqrt{\epsilon_2(\omega)}$, with $\epsilon_2(\omega)$ the substrate dielectric function. For Sa, we use the dispertion relation of the refractive index $n_2(\omega)$. According to the C_{6v} point group symmetry of SLG on a substrate [40], the relative angle between laser polarization and SLG lattice is not important for the third-order response (see Supplementary Information Sect.S2.2). We can thus assume the incident light polarization $\hat{\ell}$ along the zigzag direction without loss of generality. $\sigma^{(3)}_{\ell\ell\ell\ell}$ can then be calculated employing a diagrammatic technique [22, 26, 35], where we evaluate a four-leg Feynman diagram for the TH response function (see Supplementary Information Sect.S2 and Supplementary Fig.2). The light-matter interaction is considered in a scalar potential gauge in order to capture all intra-, inter-band and mixed transitions [21, 22, 34].

The THGE is proportional to $I^2_{\omega_0}$, Eq.2. Thus, the THG intensity scales with $I^3_{\omega_0}$, Fig.S11. The $I^2_{\omega_0}$ dependence indicates that the THGE of different experiments should not be directly compared, since differences in average power, spot size, pulse duration, repetition rate etc. will strongly affect its value. As stressed in Ref.36, it is hard to precisely quantify the efficiency of nonlinear effects in SLG. This is because one typically deals with optical powers of the nonlinear signal$\sim$1-100fW, for which background subtraction becomes critical. The $I^2_{\omega_0}$ dependence makes it even more difficult to estimate the THGE absolute value. The estimate of the losses of the optical setups also introduces uncertainty. In order to compare our results with literature, we use the third order nonlinear susceptibility $\chi^{(3)}$. There is a large discrepancy in the reported SLG $\chi^{(3)}$, from$\sim10^{-16}\mathrm{m^2V^{-2}}$ [36] to$\sim10^{-19}\mathrm{m^2V^{-2}}$ [41]. Note that these studies modeled $\chi^{(3)} \equiv i\sigma^{(3)}/(3\epsilon_0\omega_0 d_{eff})$ [34], by considering SLG with a thickness d_{eff}. This approach is incorrect because the effective susceptibilities are well defined only in three-dimensional materials, since they involve a polarization per unit volume [26]. Here we model directly $\sigma^{(3)}$, therefore we do not need to use d_{eff}. By using the same model as Ref.36, we get $\chi^{(3)} \sim5\times10^{-18}\mathrm{m^2V^{-2}}$ at $\hbar\omega_0 \sim0.7$eV and $\chi^{(3)} \sim8\times\mathrm{x}10^{-17}\mathrm{m^2V^{-2}}$ at $\hbar\omega_0 \sim0.4$eV for SLG on Sa ($|E_F| \sim250$meV). This is one order of magnitude smaller than Ref.36. However, $\chi^{(3)}$ in ref.36 is 1-3 orders of magnitude larger than any other THG experiments on SLG [26, 41].

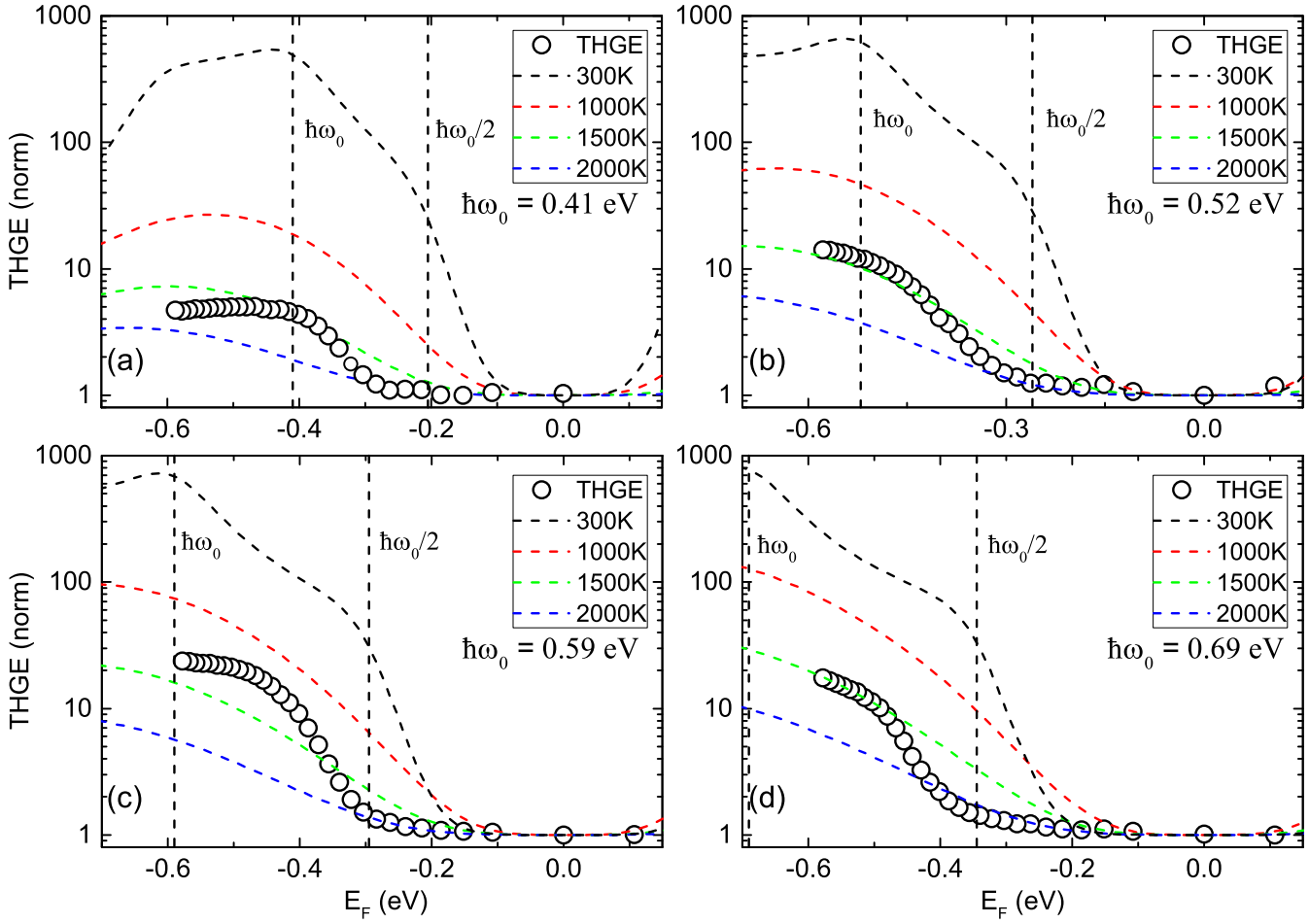

Figure 4: **Broadband THGE electrical modulation.** Experiments (circles) and theory (dotted lines) for THGE as a function of E_F, T_e for SLG on Si/SiO_2 at incident photon energies of (a)0.41, (b)0.52, (c)0.59, (d)0.69eV. The vertical dotted lines in each panel are at $|E_F| = \hbar\omega_0/2$ and $\hbar\omega_0$.

Electronic temperature. Both E_F and T_e play a key role in THGE. Fig.3b indicates that T_e is well above RT during the THG experiments. The experimental enhancement between 0.69eV and 0.41eV is$\sim$68. From the theoretical curves (dotted lines) in Fig.3b, the enhancement between 0.69eV and 0.41eV is$\sim$1400 at T_e=300K,$\sim$180 at 1000K,$\sim$65 at 2000K and$\sim$50 at 3000K. This indicates that T_e is in the range 1000-2000K. Fig.4 compares experiments and theory for THGE for four $\hbar\omega_0$ between 0.41 and 0.69eV and different T_e. Each curve, both theoretical (dotted lines) and experimental (white circles), is normalized by its minimum value to highlight the V_G dependent enhancement of THGE at different T_e. Both theory and experiments display a plateau-like feature for THGE at low $|E_F|$ ($2|E_F| < \hbar\omega_0$), which corresponds to inter-band transitions. By further increasing $|E_F|$, we reach the energy region for intra-band transitions ($\hbar\omega_0 < 2|E_F|$), where we observe a THGE rise up to a maximum for $|E_F| \sim 1.25\hbar\omega_0$ (Fig.4a). This is due to the merging of the two T_e=0K resonances at $|E_F|/\hbar\omega_0$ =1 and 1.5 as a result of high T_e (see Supplementary Information Sect.S2.4 and Supplementary Fig.5,6). Fig.4 again indicates that the best agreement between theory and experiments is reached when $\sim$1000K$\leq T_e \leq$2000K, consistent with Fig.3b. The data for all incident photon energies are well reproduced by the theoretical curves at T_e=2000K for $|E_F| < \hbar\omega_0/2$. For $|E_F| > \hbar\omega_0/2$ the data are better reproduced by theoretical curves with lower T_e $\sim$1000-1500K. This can be understood by taking into account the dependence of the linear absorption of SLG on $\hbar\omega_0$, E_F and T_e, as discussed in the Supplementary Information Sect.3,4. For finite T_e (>300K) inter-band transitions can occur also when $\hbar\omega_0 < 2E_F$ due to thermal broadening of the SLG Fermi-Dirac distribution (see Supplementary Information Sect.S4.1). Intra-band transitions also contribute to an increase of T_e, especially when $\hbar\omega_0 < 2E_F$.

T_e can also be estimated as follows. When a pulse of duration Δt and fluence $\mathcal{F}$, with average absorbed power per unit area P/A, photoexcites SLG, the variation dU of the energy density in a time interval dt is dU=(P/A)dt. The corresponding T_e increase is $dT_e = dU/c_v$, where c_v is the electronic heat capacity of the photoexcited SLG, as derived in Supplementary Information Sect.S3 and Supplementary Fig.7,8. When the pulse is off, T_e relaxes towards the lattice temperature on a time-scale τ. This reduces T_e by $dT_e = -(T_e/\tau)dt$ in a time interval dt. Thus:

$$\frac{dT_e}{dt} = \frac{\alpha}{c_v}\frac{\mathcal{F}}{\Delta t} - \frac{T_e - T_0}{\tau} \tag{3}$$

where T_0 is the initial temperature. If the pulse duration is: (i) much longer than$\sim$20fs, which is the time-scale for the electron distribution to relax to the Fermi-Dirac profile in both bands [42, 43]; (ii) comparable to the time-

scale$\sim$ $150-200fs$ needed to heat the optical phonon modes [42–45], T_e reaches a steady-state during the pulse, given by:

$$T_e = T_0 + \tau \frac{\alpha}{c_v(\mu_c, \mu_v, T_e)} \frac{\mathcal{F}}{\Delta t} \ . \tag{4}$$

α and the T_e dependence of C_v in Eq.4 are described in Supplementary Information Sect.S3,4. In our experiments: $\mathcal{F}$=70μJ/cm^2 and Δt=300fs. Based on this model $T_e \sim$ 1000-1500K for $|E_F| < \hbar\omega_0/2$ and $\sim$500K for $E_F \gg \hbar\omega_0/2$ if the residual intra-band absorption is 0.1%, as shown in Supplementary Information Sect.4.2 and Supplementary Fig.9-11. This is in good agreement with the THGE in Fig.4, where we see a reduction of 25-50% of T_e at $|E_F| = \hbar\omega_0/2$. This confirms the qualitative trend of THGE as a function of T_e.

Conclusions. The THGE efficiency in SLG can thus be modulated by over one order of magnitude by controlling its E_F and by almost two orders of magnitude by tuning the incident photon energy in the range$\sim$0.4-0.7eV. The observation of a steep increase of THGE at $|E_F|$=$\hbar\omega_0/2$ for all the investigated photon energies suggests that the effect can be observed over the entire linear bandwidth of the SLG massless Dirac fermions. These results pave the way to novel SLG-based nonlinear photonic devices, in which the gate tuneability of THG may be exploited to implement on-chip schemes for optical communications and signal processing, such as ultra-broadband frequency converters.

References

[1] Shen, Y. R. *The Principles of Nonlinear Optics* (John Wiley & Sons, New York, 1984).

[2] Butcher, P. N. & Cotter D. *The Elements of Nonlinear Optics* (Cambridge university press, London, 1991).

[3] Franken, P. A., Hill, A. E., Peters, C. W. & Weinreich, G. Generation of optical harmonics. *Phys. Rev. Lett.* **7,** 118 (1961).

[4] Stolen, R. H., Bjorkholm, J. E. & Ashkin, A. Phase-matched three-wave mixing in silica fiber optical waveguides. *Appl. Phys. Lett.* **24,** 308 (1974).

[5] Armstrong, J. A., Bloembergen, N., Ducuing, J. & Pershan, P. S. Interactions between light waves in a nonlinear dielectric. *Phys. Rev.* **127,** 1918 (1962).

[6] Steinmeyer, G., Sutter, D. H., Gallmann, L., Matuschek, N. & Keller, U. Frontiers in ultrashort pulse generation: pushing the limits in linear and nonlinear optics. *Science* **286,** 1507 (1999).

[7] Chang, J. J., Warner, B. E., Dragon, E. P. & Martinez, M. W. Precision micromachining with pulsed green lasers. *J. Laser Appl.* **10,** 285 (1998).

[8] Garmire, E. Nonlinear optics in daily life. *Opt. Express* **21,** 30532 (2013).

[9] Miller, G. D. *et al.* 42%-efficient single-pass cw second-harmonic generation in periodically poled lithium niobate. *Opt. Lett.* **22,** 1834 (1997).

[10] Cerullo, G. & De Silvestri, S. Ultrafast optical parametric amplifiers. *Rev. Sci. Instrum.* **74,** 1 (2003).

[11] Bosenberg, W. R., Drobshoff, A., Alexander, J. I., Myers, L. E. & Byer, R. L. 93% pump depletion, 3.5-W continuous-wave, singly resonant optical parametric oscillator. *Opt. Lett.* **21,** 1336 (1996).

[12] Corkum, P. B. Plasma perspective on strong field multiphoton ionization. *Phys. Rev. Lett.* **71,** 1994 (1993).

[13] Corkum, P. B. & Krausz, F. Attosecond science. *Nat. Phys.* **3,** 381 (2007).

[14] Ferguson, B. & Zhang, X.-C. Materials for terahertz science and technology. *Nat. Mater.* **1,** 26 (2002).

[15] Shcherbakov M. R. *et al.*, Enhanced third-harmonic generation in silicon nanoparticles driven by magnetic response. *Nano. Lett.* **14,** 6488 (2014).

[16] Chen, R., Lin, D. L. & Mendoza, B. Enhancement of the third-order nonlinear optical susceptibility in Si quantum wires. *Phys. Rev. B* **48,** 11879 (1993).

[17] Tsang, T. Y. F. Surface-plasmon-enhanced third-harmonic generation in thin silver films. *Opt. Lett.* **21,** 245 (1996).

[18] Cai, W., Vasudev, A.P., Brongersma, M.L. Electrically Controlled Nonlinear Generation of Light with Plasmonics. *Science* **6050,** 1720 (2011).

[19] Corcoran, B. *et al.* Green light emission in silicon through slow-light enhanced third-harmonic generation in photonic-crystal waveguides. *Nat. Photon.* **3,** 206 (2009).

[20] Seyler, K. L. *et al.* Electrical control of second-harmonic generation in a WSe_2 monolayer transistor. *Nat. Nanotech.* **10,** 407 (2015).

[21] Mikhailov, S. A. Quantum theory of the third-order nonlinear electrodynamic effects of graphene. *Phys. Rev. B* **93,** 085403 (2016).

[22] Rostami, H. & Polini, M. Theory of third-harmonic generation in graphene: A diagrammatic approach. *Phys. Rev. B* **93,** 161411 (2016).

[23] Hendry, E., Hale, P. J., Moger, J., Savchenko A. K. & Mikhailov, S. A. Coherent nonlinear optical response of graphene. *Phys. Rev. Lett.* **105,** 097401 (2010)

[24] Wang, G. *et al.* Giant enhancement of the optical second-harmonic emission of WSe_2 monolayers by laser excitation at exciton resonances. *Phys. Rev. Lett.* **114,** 097403 (2015).

[25] Liu, H. *et al.* High-harmonic generation from an atomically thin semiconductor. *Nat. Phys.* **13,** 262 (2017).

[26] Saynatjoki, A. *et al.* Ultra-strong nonlinear optical processes and trigonal warping in MoS_2 layers. *Nat Comms* **8,** 893 (2017)

[27] Klein, J. *et al.* Electric-field switchable second-harmonic generation in bilayer MoS_2 by inversion symmetry breaking. *Nano Lett.* **17,** 392 (2017).

[28] Sun, Z. *et al.* Graphene mode-locked ultrafast laser. *ACS Nano* **4,** 803 (2010).

[29] Bonaccorso, F., Sun, Z., Hasan, T. & Ferrari, A. C. Graphene photonics and optoelectronics. *Nat. Photon.* **4,** 611 (2010).

[30] Mikhailov, S. A. Theory of the giant plasmon-enhanced second-harmonic generation in graphene and semiconductor two-dimensional electron systems. *Phys. Rev. B* **84,** 045432 (2011).

[31] Dean, J. J. & van Driel, H. M. Graphene and few-layer graphite probed by second-harmonic generation: Theory and experiment. *Phys. Rev. B* **82,** 125411 (2010).

[32] An, Y. Q., Nelson, F., Lee, J. U. & Diebold, A. C. Enhanced optical second-harmonic generation from the current-biased graphene/SiO_2/Si(001) structure. *Nano Lett.* **13,** 2104 (2013).

[33] An, Y. Q., Rowe, J. E., Dougherty, D. B., Lee, J. U. & Diebold, A. C. Optical second-harmonic generation induced by electric current in graphene on Si and SiC substrates. *Phys. Rev. B* **89,** 115310 (2014).

[34] Cheng, J. L, Vermeulen, N. & Sipe, J. E. Third order optical nonlinearity of graphene. *New J. Phys.* **16,** 053014 (2014);

[35] Rostami, H., Katsnelson, M. I. & Polini, M. Theory of plasmonic effects in nonlinear optics: The case of graphene. *Phys. Rev. B* **95,** 035416 (2017).

[36] Kumar, N. *et al.* Third harmonic generation in graphene and few-layer graphite films. *Phys. Rev. B* **87,** 121406(R) (2013).

[37] Alexander, K., Savostianova, N. A., Mikhailov, S. A., Kuyken, B. & Van Thourhout, D. Electrically tuneable optical nonlinearities in graphene-covered SiN waveguides characterized by four-wave mixing. *ACS Photonics* **4,** 3039 (2017).

[38] Casiraghi, C. *et al.* Rayleigh imaging of graphene and graphene layers. *Nano Lett.* **7,** 2711 (2007).

[39] Mak, K. F. *et al.* Measurement of the optical conductivity of graphene. *Phys. Rev. Lett.* **101,** 196405 (2008).

[40] Mañes, J. L. Symmetry-based approach to electron-phonon interactions in graphene. *Phys. Rev. B* **76**, 045430 (2007).

[41] Woodward, R.I. *et al.* Characterization of the second- and third-order nonlinear optical susceptibilities of monolayer MoS_2 using multiphoton microscopy. *2D Mater.* **4,** 011006 (2017).

[42] Brida, D. *et al.* Ultrafast collinear scattering and carrier multiplication in graphene. *Nat. Comms.* **4,** 1987 (2013)

[43] Breusing, M. *et al.* Ultrafast nonequilibrium carrier dynamics in a single graphene layer. *Phys. Rev. B* **83,** 153410 (2011).

[44] Lazzeri, M., Piscanec, S., Mauri, F., Ferrari, A. C. & Robertson, J. Electron transport and hot phonons in carbon nanotubes. *Phys. Rev. Lett.* **95,** 236802 (2005).

[45] Piscanec, S., Lazzeri, M., Mauri, F., Ferrari, A. C., & Robertson, J. Kohn anomalies and electron-phonon interactions in graphite. *Phys. Rev. Lett.* **93,** 185503 (2004)

Acknowledgements

We acknowledge funding from EU Graphene Flagship, ERC Grant Hetero2D, EPSRC Grants EP/K01711X/1, EP/K017144/1, EP/N010345/1, and EP/L016087/1.

Authors contributions

A.C.F, G.C. and G.S. conceived and designed the experiment. G.S. and G.W. prepared the experimental setup. G.S., G.W, S.D.C., M.C. and S.B. performed the THG experiments. G.S. analysed the THG data. A.O. and D.Y. measured the Raman spectra. D.P., T.M., B.L., J. W., J.E.M., I.G. prepared the samples. H.R. and A.T. developed the THG theory and model for T_e. G.S., A.C.F., G.C. and M.P. wrote the paper, with input from all authors.

Competing interests

The authors declare no competing financial interests.

Supplementary information

Supplementary information is available in the online version of the paper. Reprints and permission information is available online at www.nature.com/reprints. Correspondence and requests for materials should be addressed to G.S. and A.C.F.

Methods

Samples preparation and characterization

SLG on Sa is prepared as follows. SLG is grown by CVD on Cu as for Ref. [46]. A Cu foil (99.8% pure) substrate is placed in a furnace. Annealing is performed at 1000 °C in a 20sccm (standard cubic centimeters per minute) hydrogen atmosphere at ∼196mTorr for 30min. Growth is then initiated by introducing 5sccm methane for 30mins. The resulting film is characterized by Raman spectroscopy [47, 48] with a Horiba Labram HR800 spectrometer equipped with a 100x objective at 514nm, with a power on the sample∼500μW to avoid any possible heating effects. The D to G intensity ratio is I(D)/I(G)$\ll$0.1, corresponding to a defect density $n_D \ll 2.4 \times 10^{10}$cm^{-2} [49, 50]. The 2D peak position (Pos) and full width at half maximum (FWHM) are Pos(2D)∼2703cm^{-1} and FWHM(2D)∼36cm^{-1}, respectively, while Pos(G)∼1585cm^{-1} and FWHM(G)∼18cm^{-1}. The 2D to G intensity and area ratios are I(2D)/I(G)∼3.3 and A(2D)/A(G)∼6.5, respectively. The CVD SLG is then transferred on Sa by polymer-assisted Cu wet etching [51], using polymethyl methacrylate (PMMA). After transfer Pos(2D)∼2684cm^{-1}, FWHM(2D)∼24cm^{-1}, Pos(G)∼1584cm^{-1}, FWHM(G) ∼13cm^{-1}, I(2D)/I(G)∼5.3, A(2D)/A(G)∼10. From Refs.52, 53 we estimate E_F ∼250meV. After transfer, I(D)/I(G)∼0.14, which corresponds to $n_D \sim 6.0 \times 10^{10}$cm^{-2} [49, 50] with a small increase of defect density.

The back-gated SLG sample is prepared by micromechanical exfoliation of graphite on Si+285nm SiO_2 [54]. Suitable single-layer flakes are identified by optical microscopy [38] and Raman spectroscopy [47, 48]. The device is then prepared as follows. We deposit a resist (A4-495) on the exfoliated SLG on Si/SiO_2 and pattern it with electron beam lithography. Then, we develop the resist in a solution of isopropanol (IPA) diluted with distilled water, evaporate and lift-off 5/70nm of Cr/Au. Cr is used to improve adhesion of the Au, while Au is the metal for source-drain contacts. Raman spectroscopy is then performed after processing. We get Pos(2D)∼2678cm^{-1}, FWHM(2D)∼25cm^{-1}, Pos(G)∼1581cm^{-1}, FWHM(G)∼12cm^{-1}, I(2D)/I(G) ∼4.9, A(2D)/A(G)∼10.3, indicating E_F <100meV [52, 53]. I(D)/I(G)$\ll$0.1, corresponding to $n_D \ll 2.4 \times 10^{10}$cm^{-2} [49, 50].

When V_G is applied, E_F is derived from V_G as follows [52]:

$$E_F = \hbar v_F \sqrt{\pi n} \tag{5}$$

where $\hbar$ is the reduced Plank constant, and n is the SLG carrier concentra-

tion. This can be written as [52]:

$$n = \frac{C_{\rm BG}}{e}(V_{\rm G} - V_0) \tag{6}$$

where $C_{BG} = \epsilon\epsilon_0/d_{BG} = 1.2 \times 10^{-8}$Fcm^{-2} is the back-gate capacitance (d_{BG}=285nm is the back-gate thickness and $\epsilon \sim 4$ the SiO_2 dielectric constant [52]), $e > 0$ is the fundamental charge and V_0 is the voltage at which the resistance of the SLG back-gated device reaches its maximum (minimum of the current between source and drain). We note that the SLG quantum capacitance (C_{QC}) is negligible in this context. The SiO_2 layer and SLG can be considered as two capacitors in series and the SLG C_{QC} is $\sim 10^{-6}$Fcm^{-2} [55]. Thus, the total capacitance $C_{tot} = (1/C_{BG} + 1/C_{QC})^{-1} \sim C_{BG}$.

THGE measurements and calibration

THGE measurements are performed in air at room temperature for both transmission and reflection, as shown in Fig.2. For excitation we use the idler beam of an OPO (Coherent) tuneable between$\sim$0.31eV (4μm) and$\sim$0.73eV (1.7μm). This is seeded by a mode-locked Ti:Sa laser (Coherent) with 150fs pulse duration, 80MHz repetition rate and 4W average power at 800nm. The OPO idler is focused by a 40X reflective objective (Ag coating, numerical aperture NA=0.5) to avoid chromatic aberrations. The THG signal is collected by the same objective (in reflection mode) or collimated by an 8mm lens (in transmission mode) and delivered to a spectrometer (Horiba iHR550) equipped with a nitrogen cooled Si CCD. The idler spot-size is measured with the razor-blade technique to be$\sim 4.7\mu$m. This corresponds to an excitation fluence$\sim 70\mu$J/cm^2 for the average power (1mW) used in our experiments. The idler pulse duration is checked by autocorrelation measurements, based on two-photon absorption on a single channel Si photodetector, and is$\sim$300fs. Under these conditions, the THG signal is stable over at least 1 hour. For the V_G dependent THGE measurements we use a Keithley 2612B dual channel source meter to apply V_G between -150 and +150V, a source-drain voltage (10mV), as well as to read the source-drain current (I_{SD}). For the photon energy dependence measurements we use 60s acquisition time and 10 accumulations (giving a total of 10 minutes for each spectrum). For the gate dependence measurements we proceed as follows. We tune $V_{\rm G}$ (62 points between -150 and +150V) and for each V_G we measure the THG signal by using 10s acquisition time and 1 accumulation. We use a shorter accumulation time compared to the photon energy measurements to reduce the total time required for each $V_{\rm G}$ scan. A lower accumulation time implies that less photons are collected by the CCD. We consider the amplitude of THG in

counts/s, by dividing the number of counts detected on the CCD by the accumulation time. Thus, in the case of V_G dependent measurements, SLG is kept at a given V_G for 10s before moving to the next point (next value of V_G). This corresponds to$\sim$10minutes for each measurement (*i.e.* a full V_G scan between -150 and + 150V). In this way, for each V_G and, consequently, for each E_F, we record one THG signal spectrum.

To estimate the ω_0 dependent THGE, it is necessary to first characterize the photon energy dependent losses of the optical setup. The pump-power is measured on the sample (by removing it and measuring the power after the objective). The major losses along the optical path are the absorption of Sa, the grating efficiency, and the CCD quantum efficiency. We also need to consider the CCD gain. The Sa transmittance is$\sim$85% in the energy range of our THG experiments. To evaluate the losses of the grating and the absorption of the CCD, we align the Ti:Sa laser, tuneable between$\sim$1.2 and 1.9eV ($\sim$650-1050nm), with the microscope and detect it on the CCD. We then measure the signal on the spectrometer, given a constant number of photons for all wavelengths, and compare this with the spectrometer specifications. The spectrometer used in our setup is a Horiba Symphony II 1024 x 256 with Cryogenic Open-Electrode CCD Detector. The quantum Efficiency and grating (300 gr/mm , Blazed 600 nm 510 19 140) relative efficiency are available from the Horiba website. We get an excellent agreement between the two methods (*i.e.* evaluation of the losses from detection of the fundamental beam and spectrometer specifications). Thus we use the spectrometer specifications to estimate the losses due to grating and CCD efficiencies. We also account for the CCD gain, *i.e.* the number of electrons necessary to have 1 count. The instrument specifications give a gain$\sim$7.

Data availability

The data that support the plots within this paper and other findings of this study are available from the corresponding authors upon reasonable request.

References

[46] Li, X. S. *et al.*, Large-area synthesis of high-quality and uniform graphene films on copper foils. *Science* **324,** 1312 (2009).

[47] Ferrari A. C. & Basko, D. M. Raman spectroscopy as a versatile tool for studying the properties of graphene. *Nat. Nanotechnol.* **8,** 235 (2013).

[48] Ferrari, A. C. *et al.* Raman spectrum of graphene and graphene layers. *Phys. Rev. Lett.* **97,** 187401, (2006).

[49] Cancado, L. G. *et al.* Quantifying defects in graphene via Raman spectroscopy at different excitation energies. *Nano Lett.* **11,** 3190 (2011).

[50] Bruna, M. *et al.* Doping dependence of the Raman spectrum of defected graphene. *ACS Nano* **8,** 7432 (2014)

[51] Bonaccorso, F. *et al.* Production and processing of graphene and 2d crystals. *Mater. Today* **15,** 564 (2012).

[52] Das, A. *et al.*, Monitoring dopants by Raman scattering in an electrochemically top-gated graphene transistor. *Nat. Nanotechnol.* **3,** 210 (2008)

[53] Basko, D. M., Piscanec, S. & Ferrari, A. C. Electron-electron interactions and doping dependence of the two-phonon Raman intensity in graphene. *Phys. Rev. B* **80,** 165413 (2009).

[54] Novoselov, K. S. *et al.* Two-dimensional atomic crystals. *Proc. Natl. Acad. Sci. U.S.A* **102,** 10451 (2005).

[55] Xia, J., Chen, F., Li, J. & Tao, N. Measurement of the quantum capacitance of graphene. *Nat. Nanotechnol.* **4,** 505 (2009).